

Reconfigurable microring resonators for multipurpose quantum light sources

Yuxing Du(杜昱星), Yingwen Liu(刘英文), Chao Wu(吴超), Pingyu Zhu(朱枰谕), Chang Zhao(赵畅), Miaomiao Yu(余苗苗), Yan Wang(王焱), Kaikai Zhang(张凯凯), and Ping Xu(徐平)

Citation: Chin. Phys. B, 2025, 34 (**7**): 074207. DOI: 10.1088/1674-1056/adcc88
http://cpb.iphy.ac.cn; http://iopscience.iop.org/cpb

What follows is a list of articles you may be interested in

Four-wave mixing Bragg scattering for small frequency shift from silicon coupled microrings

Chang Zhao(赵畅), Chao Wu(吴超), Pingyu Zhu(朱枰谕), Yuxing Du(杜昱星), Yan Wang(王焱), Miaomiao Yu(余苗苗), Kaikai Zhang(张凯凯), and Ping Xu(徐平)

Chin. Phys. B, 2025, 34 (**1**): 014206. DOI: 10.1088/1674-1056/ad8a4f

Engineering the spectra of photon triplets generated from micro/nanofiber

Chuan Qu(瞿川), Dongqin Guo(郭东琴), Xiaoxiao Li(李笑笑), Zhenqi Liu(刘振旗), Yi Zhao(赵义), Shenghai Zhang(张胜海), and Zhengtong Wei(卫正统)

Chin. Phys. B, 2024, 33 (**3**): 034208. DOI: 10.1088/1674-1056/ad1c5d

High-performance and fabrication friendly polarization demultiplexer

Huan Guan(关欢), Yang Liu(刘阳), and Zhiyong Li (李智勇)

Chin. Phys. B, 2022, 31 (**3**): 034203. DOI: 10.1088/1674-1056/ac21bc

Bandwidth-tunable silicon nitride microring resonators

Jiacheng Liu(刘嘉成), Chao Wu(吴超), Gongyu Xia(夏功榆), Qilin Zheng(郑骑林), Zhihong Zhu(朱志宏), and Ping Xu(徐平)

Chin. Phys. B, 2022, 31 (**1**): 014201. DOI: 10.1088/1674-1056/ac2e64

Highly sensitive digital optical sensor with large measurement range based on the dual-microring resonator with waveguide-coupled feedback

Xiang Xing-Ye (向星烨), Wang Kui-Ru (王葵如), Yuan Jin-Hui (苑金辉), Jin Bo-Yuan (晋博源), Sang Xin-Zhu (桑新柱), Yu Chong-Xiu (余重秀)

Chin. Phys. B, 2014, 23 (**3**): 034206. DOI: 10.1088/1674-1056/23/3/034206

Reconfigurable microring resonators for multipurpose quantum light sources

Yuxing Du(杜昱星)[†], Yingwen Liu(刘英文)[†], Chao Wu(吴超), Pingyu Zhu(朱枰谕), Chang Zhao(赵畅), Miaomiao Yu(余苗苗), Yan Wang(王焱), Kaikai Zhang(张凯凯), and Ping Xu(徐平)[‡]

College of Computer Science and Technology, National University of Defense Technology, Changsha 410073, *China*

(Received 22 March 2025; revised manuscript received 10 April 2025; accepted manuscript online 15 April 2025)

Microring resonators (MRRs) are extensively utilized in photonic chips for generating quantum light sources and enabling high-efficiency nonlinear frequency conversion. However, conventional microrings are typically optimized for a single specific function, limiting their versatility in multifunctional applications. In this work, we propose a reconfigurable microring resonator architecture designed to accommodate diverse application requirements. By integrating a cascaded Mach–Zehnder interferometer (MZI) as the microring coupler, the design enables independent control of the quality factors for pump, signal and idler photons through two tunable phase shifters. This capability allows for dynamic tuning and optimization of critical performance parameters, including photon-pair generation rate (PGR), spectral purity and single photon heralding efficiency (HE). The proposed structure is implemented on a silicon photonic chip, and experimental results exhibit a wide range of tunability for these parameters, with excellent agreement with theoretical predictions. This flexible and multi-functional design offers a promising pathway for high-performance, highly integrated on-chip quantum information processing systems.

Keywords: microring resonators, cascaded Mach–Zehnder interferometer, quantum light sources

PACS: 42.65.–k, 42.65.Wi, 42.82.–m, 42.82.Et

DOI: 10.1088/1674-1056/adcc88 **CSTR:** 32038.14.CPB.adcc88

1. Introduction

Quantum light sources are fundamental components in the field of quantum information science and technology, playing a critical role in quantum communication,[1] quantum computing,[2] and quantum sensing.[3] With the rapid advancement of integrated photonics, the integration of quantum light sources onto silicon-based chips to develop efficient, compact, and scalable quantum optical systems has become a prominent research direction.[4,5] Silicon photonic chips, with their compatibility with mature CMOS fabrication processes, low cost, and high integration density, offer tremendous potential for enabling practical quantum technologies.[6–8]

Currently, leveraging the relatively high third-order nonlinear coefficient of silicon, research on silicon-based quantum light sources primarily focuses on the spontaneous four-wave mixing (SFWM) process,[4,9,10] achieving significant progress in photon-pair generation. However, silicon-based photon-pair sources still face limitations in key performance metrics, such as generation efficiency, spectral purity, and tunability, particularly when compared to sources based on second-order nonlinear processes like spontaneous parametric down-conversion (SPDC).[11,12] To address these challenges, hybrid designs incorporating asymmetric Mach–Zehnder interferometers (AMZI) and MRR have garnered increasing attention.[13,14] This architecture enhances SFWM efficiency[15] through the field-enhancement effect of microring resonators while enabling dynamic control of coupling coefficients via interference effects, thereby offering flexible tunability to optimize source performance.[16,17]

For instance, a reconfigurable microring resonator structure was proposed in Ref. [10], where the AMZI interference effect was utilized to regulate the quality factor, enabling the optimization of nonlinear frequency conversion and photon-pair generation rates. However, in this design, the coupling coefficients of adjacent resonance wavelengths remained identical, resulting in non-independent control of the quality factors for the pump, signal, and idler modes. This constraint prevents the design from achieving the theoretically optimal values attainable with independent quality factor control, limiting its ability to adjust photon spectral purity.

More advanced approaches, such as using double-AMZI coupled MRRs, have been shown to enable independent tuning of the quality factors for the pump and signal (or idler) modes. For example, in Ref. [18], this design achieved a photon spectral purity exceeding the conventional theoretical limit, reaching $95\% \pm 1.5\%$. However, in this case, the coupling coefficients for the pump and signal (or idler) modes were still dictated by the fixed coupling gap between the MRR and AMZI, necessitating the fabrication of multiple structures with varying coupling distances to explore differ-

[†]These authors contributed equally to this work.

[‡]Corresponding author. E-mail: pingxu520@nju.edu.cn

© 2025 Chinese Physical Society and IOP Publishing Ltd. All rights, including for text and data mining, AI training, and similar technologies, are reserved.

ent operating conditions. From the above analysis, it is evident that conventional AMZI-MRR coupled structures typically focus on optimizing a single performance metric, such as high-brightness quantum light sources,[19,20] high-purity quantum state generation,[21,22] or high-efficiency frequency conversion.[23] However, these designs do not allow for independent control over the quality factors of the pump and signal (or idler) photons, thereby limiting their potential for use in versatile quantum photonic devices.

In the present research, we propose an innovative design that combines a microring resonator with a cascaded asymmetric Mach–Zehnder interferometer. By leveraging the interference characteristics of the cascaded AMZI, the proposed architecture enables independent and wide-ranging control of the quality factors for the pump, signal, and idler modes. This design dynamically adjusts the nonlinear interactions of the four optical fields involved in the SFWM processes, allowing for the tailored optimization of quantum light source performance to meet different application requirements. This approach provides a novel and versatile pathway for realizing multifunctional, general-purpose on-chip quantum light sources, offering significant potential for advancing integrated quantum photonic technologies.

2. Theoretical method

In this work, we designed and fabricated an MRR coupled with cascaded AMZI, as shown in Fig. 1(a). In this structure, a curved optical waveguide forms three coupling regions with a micro-ring, and these regions collectively behave as a cascaded Mach–Zehnder interferometer. The structure as observed under the microscope is shown in the Fig. 1(c). The pump light is injected at one end of the curved waveguide, where energy is exchanged between the waveguide and the micro-ring at the coupling regions, ultimately resulting in the output of the optical field from the other end of the waveguide. The overall coupling effect between the waveguide and the microring is determined by the interference effects of the cascaded interferometers. Specifically, when the two light paths in the interferometer interfere constructively at the output port, the transmission rate is maximized, and the overall coupling effect is weakest. Conversely, when the two light paths interfere destructively at the output port, the overall coupling effect is strongest. The coupling gaps g of the three coupling regions are identical, ensuring that the directional couplers have the same self-coupling coefficient t and cross-coupling coefficient κ, satisfying the relation $t^2+\kappa^2=1$. The arm length difference of each AMZI is ΔL, and each long-arm waveguide is integrated with thermo-optic modulators for phase tuning, which are represented as θ_1 and θ_2, respectively.

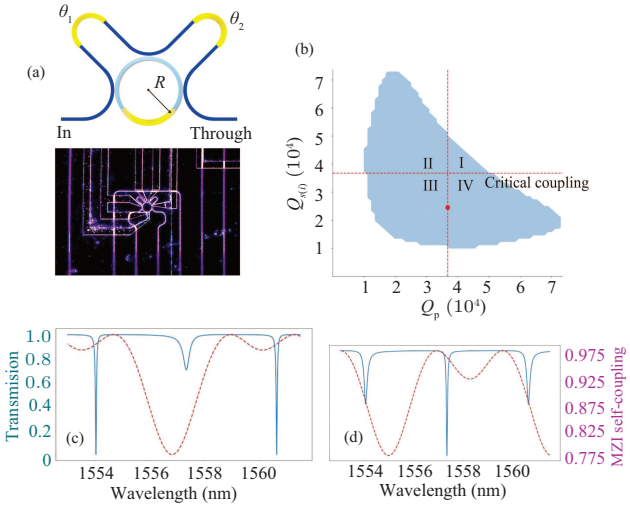


Fig. 1. (a) Schematic diagram of the cascaded AMZI-coupled microring resonator. The long and short arm lengths of the two interferometers are identical, with an arm length difference of $\Delta l=\pi R$. Three thermo-optic phase shifters are integrated to independently control the interferometer phases (θ_1,θ_2) and the microring resonance. (b) Chip architecture observed under an electron microscope. (c) Theoretical tunable ranges of $Q_{\rm p}$ and $Q_{\rm s(i)}$ for the cascaded AMZI-coupled microring resonator. The red dashed line indicates the critical coupling condition for both pump and signal (idler) photons; The red markers represent the theoretical maximum PGR, achieved under the condition of critical coupling for the pump light ($Q_{\rm int,p}/Q_{\rm ext,p}=1$) and overcoupling for the signal (idler) light ($Q_{\rm int,s(i)}/Q_{\rm ext,s(i)}=2$). (d) Theoretical transmission spectrum and variation of $|\kappa_{\rm e}|^2$ as a function of wavelength in region II of panel (c). (e) Theoretical transmission spectrum and variation of $|\kappa_{\rm e}|^2$ as a function of wavelength in region IV of panel (c). Due to the arm length difference of πR in the interferometer, the interference period is twice that of the microring resonance. Consequently, the signal and idler photons, separated by twice the resonance period, exhibit identical interference behavior.

We begin with the interaction Hamiltonian to derive the relationships between the photon generation rate (PGR), heralding efficiency (HE), and spectral purity under continuous-wave and pulsed pumping, in connection with the quality factors of the pump, signal, and idler photons. In general, the Hamiltonian governing the SFWM interaction can be expressed as follows:

$$H(t)=\frac{3\varepsilon_0}{4}\int \mathrm{d}\boldsymbol{r}\chi^{(3)}E_{\rm s}^{(-)}(\boldsymbol{r},t)E_i^{(-)}(\boldsymbol{r},t)E_{\rm p}^{(+)}(\boldsymbol{r},t)E_{\rm p}^{(+)}(\boldsymbol{r},t)+\text{h.c.}, \tag{1}$$

where ε_0 is the vacuum permittivity, $\chi^{(3)}$ is the third-order nonlinear coefficient, and $\mathrm{d}\boldsymbol{r}$ represents the differential volume element in the waveguide space. In the case of continuous-wave pumping, considering the resonance effects of the microring cavity, the intracavity electric field can be expressed as

$$E_{\rm p}^{(+)}(r,t)=\sqrt{\frac{2W}{\varepsilon_0 n_{\rm p} Sc}}\int\frac{\mathrm{d}\omega_{\rm p}}{\sqrt{2\pi}}f_{\rm p}\left(\omega_{\rm p}\right)l_{\rm p}\left(\omega_{\rm p}\right)\mathrm{e}^{\mathrm{i}\beta_{\rm p}z-\mathrm{i}\omega_{\rm p}t},$$

$$E_j^{(+)}(r,t) = \mathrm{i}\sqrt{\frac{\hbar\omega_{j0}}{2\varepsilon_0 n_j S c}}\int \frac{\mathrm{d}\omega_j}{\sqrt{2\pi}}\hat{a}(\omega_j) f_j(\omega_j)\,\mathrm{e}^{\mathrm{i}\beta_j z - \mathrm{i}\omega_j t}\quad (j=\mathrm{s},\mathrm{i}). \tag{2}$$

Here, W is the energy per pulse, S is the cross-sectional area of the waveguide, c is the speed of light in vacuum, $\hbar$ is the reduced Planck constant, n_j is the effective refractive index, ω_j is the central frequency. The $\hat{a}$ operators are the annihilation operators. $l_\mathrm{p}(\omega_\mathrm{p})$ is the spectral lineshape of the pump light, which satisfies the normalization condition

$$\int \mathrm{d}\omega_\mathrm{p}\left|l_\mathrm{p}(\omega_\mathrm{p})\right|^2 = 1.$$

$f_v(\omega_v)$, $(v=\mathrm{p},\mathrm{s},\mathrm{i})$ represent the resonant spectra for the pump, signal, and idler lights, respectively

$$f_v(\omega_v) = \sqrt{\frac{V_\mathrm{g}}{L}}\frac{\mathrm{i}\sqrt{2r_{\mathrm{ext},v}}}{-\mathrm{i}(\omega_v-\Omega_{v0})+r_{\mathrm{tot},v}}, \tag{3}$$

where V_g is the group velocity in the microring. The external decay rate is $r_\mathrm{ext}=\Omega_0/2Q_\mathrm{ext}$, the internal decay rate is $r_\mathrm{int}=\Omega_0/2Q_\mathrm{int}$, and the total decay rate is $r_\mathrm{tot}=r_\mathrm{ext}+r_\mathrm{int}$. Substituting the field expressions into the Hamiltonian, the interaction Hamiltonian in the microring resonator can be written as

$$\begin{aligned}H(t) = {}& \frac{\hbar\gamma WL}{(2\pi)^2}\iiiint \mathrm{d}\omega_\mathrm{s}\mathrm{d}\omega_\mathrm{i}\mathrm{d}\omega_{\mathrm{p}1}\mathrm{d}\omega_{\mathrm{p}2} f_\mathrm{s}^*(\omega_\mathrm{s}) f_\mathrm{i}^*(\omega_\mathrm{i}) f_\mathrm{p}(\omega_{\mathrm{p}1}) f_\mathrm{p}(\omega_{\mathrm{p}2}) l_\mathrm{p}(\omega_{\mathrm{p}1}) l_\mathrm{p}(\omega_{\mathrm{p}1})\\ &\times \mathrm{e}^{-\mathrm{i}(\omega_{\mathrm{p}1}+\omega_{\mathrm{p}2}-\omega_\mathrm{s}-\omega_\mathrm{i})t}\hat{a}^\dagger(\omega_\mathrm{s})\hat{a}^\dagger(\omega_\mathrm{i}) + \mathrm{h.c.},\end{aligned} \tag{4}$$

where γ is the third-order nonlinear coefficient. By inserting this Hamiltonian into the Schrödinger equation and neglecting the vacuum state, the two-photon state function generated by SFWM in the microring resonator can be derived as

$$|\psi\rangle = \frac{\gamma WL}{2\pi}\iint \mathrm{d}\omega_\mathrm{s}\mathrm{d}\omega_\mathrm{i}\phi(\omega_\mathrm{s},\omega_\mathrm{i}) a^\dagger_{\omega_\mathrm{s}} a^\dagger_{\omega_\mathrm{i}}|0\rangle, \tag{5}$$

where the correlation spectral distribution function for the signal and idler photons, $\phi(\omega_\mathrm{s},\omega_\mathrm{i})$, is given by

$$\phi(\omega_\mathrm{s},\omega_\mathrm{i}) = \int \mathrm{d}\omega_{\mathrm{p}1} f_\mathrm{s}^*(\omega_\mathrm{s}) f_\mathrm{i}^*(\omega_\mathrm{i}) f_\mathrm{p}(\omega_{\mathrm{p}1}) f_\mathrm{p}(\omega_\mathrm{s}+\omega_\mathrm{i}-\omega_{\mathrm{p}1}) l_\mathrm{p}(\omega_\mathrm{p}) l_\mathrm{p}(\omega_\mathrm{s}+\omega_\mathrm{i}-\omega_{\mathrm{p}1}). \tag{6}$$

In the special case where the pump light is continuous-wave, equation (5) reduces to

$$\begin{aligned}|\psi\rangle &= \gamma PL\iint \mathrm{d}\omega_\mathrm{s}\mathrm{d}\omega_\mathrm{i} f_\mathrm{p}(\omega_\mathrm{p}) f_\mathrm{p}(\omega_\mathrm{p}) f_\mathrm{s}^*(\omega_\mathrm{s}) f_\mathrm{i}^*(\omega_\mathrm{i})\delta(2\omega_\mathrm{p}-\omega_\mathrm{s}-\omega_\mathrm{i})\hat{a}^\dagger(\omega_\mathrm{s})\hat{a}^\dagger(\omega_\mathrm{i})|0\rangle\\ &= \gamma PL\int \mathrm{d}\omega_\mathrm{s} f_\mathrm{p}(\omega_\mathrm{p}) f_\mathrm{p}(\omega_\mathrm{p}) f_\mathrm{s}^*(\omega_\mathrm{s}) f_\mathrm{i}^*(2\omega_\mathrm{p}-\omega_\mathrm{s})\hat{a}^\dagger(\omega_\mathrm{s})\hat{a}^\dagger(2\omega_\mathrm{p}-\omega_\mathrm{s})|0\rangle.\end{aligned} \tag{7}$$

This results in the two-photon generation rate

$$\begin{aligned}R_\mathrm{si} &= \langle\psi\mid\psi\rangle = (\gamma PL)^2\int \mathrm{d}\omega_\mathrm{s}\left|f_\mathrm{s}(\omega_\mathrm{s})\right|^2\left|f_\mathrm{i}(2\omega_\mathrm{p}-\omega_\mathrm{s})\right|^2\left|f_\mathrm{p}(\omega_\mathrm{p})\right|^4\\ &= (\gamma PL)^2 16\pi\left(\frac{V_\mathrm{g}}{L}\right)^4\left(\frac{r_{\mathrm{ext,p}}}{r_{\mathrm{tot,p}}^2}\right)^2\frac{r_{\mathrm{ext,s}}}{r_{\mathrm{tos,s}}}\frac{r_{\mathrm{ext,i}}}{r_{\mathrm{tot,i}}}\frac{r_{\mathrm{tot,s}}+r_{\mathrm{tot,i}}}{\delta\Omega^2+(r_{\mathrm{tot,s}}+r_{\mathrm{tot,i}})^2},\end{aligned} \tag{8}$$

where $\delta\Omega$ is the resonance frequency detuning, which can be neglected. Simplifying the expression,[24] we see that the pump and signal (idler) light quality factors, as independent variables, jointly influence the PGR

$$R_\mathrm{si} = \frac{16V_\mathrm{g}^4\gamma^2P^2Q_\mathrm{p}^4Q_{\mathrm{s(i)}}^3}{\Omega_\mathrm{p}^3\pi R^2Q_{\mathrm{ext,p}}^2Q_{\mathrm{ext,s(i)}}^2}, \tag{9}$$

where R is the microring radius. According to Eq. (9), when the quality factors are independently optimized, the maximum PGR is achieved when the signal (or idler) photon is overcoupled $\left(Q_{\mathrm{int,s(i)}}/Q_{\mathrm{ext,s(i)}}=2\right)$ and the pump photon is critically coupled $\left(Q_{\mathrm{int,s(i)}}/Q_{\mathrm{ext,s(i)}}=1\right)$. Therefore, to achieve the optimal photon generation rate (PGR) under continuous-wave pumping, the structure must enable independent control over the quality factors of the pump and signal (or idler) photons. This capability is precisely what the aforementioned designs lack.

The additional losses encountered by the signal and idler photons generated in the microring resonator as they escape from the cavity into the coupling waveguide are referred to as the escape efficiency, $\Gamma_{\mathrm{s(i)}}$, and is given by

$$\Gamma_{\mathrm{s(i)}} = Q_{\mathrm{tot,s(i)}}/Q_{\mathrm{ext,s(i)}} = \frac{1}{1+1/\left(Q_{\mathrm{int,s(i)}}/Q_{\mathrm{ext,s(i)}}\right)}. \tag{10}$$

The heralding efficiency of the photon-pair source can be quantitatively expressed as

$$H_{\mathrm{s(i)}} = \frac{N_{\mathrm{cc}}}{N_{\mathrm{i(s)}}} = \frac{R_{\mathrm{si}}\eta_{\mathrm{s}}\eta_{\mathrm{i}}}{\eta_{\mathrm{i(s)}}\left(R_{\mathrm{si}}/\Gamma_{\mathrm{s(i)}} + n_{\mathrm{i(s)}}\right) + d_{\mathrm{i(s)}}}. \tag{11}$$

Here, N_{cc} is the experimentally measured coincidence count of signal and idler photon pairs, η_{s} and η_{i} are the total collection efficiencies for signal and idler photons during coincidence count measurements, respectively. $n_{\mathrm{i(s)}}$ represents the non-correlated single-photon noise, and $d_{\mathrm{i(s)}}$ denotes the dark count of the detector. It is evident that, in the absence of other losses, the upper limit of HE is determined by $\Gamma_{\mathrm{s(i)}}$, which is in turn governed by $Q_{\mathrm{tot,s(i)}}/Q_{\mathrm{ext,s(i)}}$.

We now examine how different quality factors influence the photon purity generated within the microring resonator. From the correlation spectral distribution function of the signal and idler photons (Eq. (6)), it is evident that the correlation between the signal and idler photons causes the detection of one photon to induce the other photon to be in a mixed state. Therefore, it is essential to minimize the degree of correlation between the signal and idler photons as much as possible, ensuring that the heralded photon is in a pure state. When the pump light is pulsed and the pump light spectral lineshape $f_{\mathrm{p}}(\omega_{\mathrm{p}})$ follows a Gaussian distribution, the resonance spectrum $l(\omega) = \mathrm{i}\kappa/(1 - t\cdot \mathrm{e}^{\mathrm{i}\beta(\omega)L}\cdot \mathrm{e}^{-\alpha L})$ in the microring adopts a Lorentzian lineshape, the spectral purity of heralded single photons can be quantified using the Schmidt number K[25] expressed as $p = 1/K$. The Schmidt number is defined as follows:

$$K = \frac{X^2}{Y},\ X = \int \mathrm{d}\omega_{\mathrm{s}} \int \mathrm{d}\omega_{\mathrm{i}} \left|\phi\left(\omega_{\mathrm{s}}, \omega_{\mathrm{i}}\right)\right|^2,\ Y = \int \mathrm{d}\omega_{\mathrm{s}} \int \mathrm{d}\omega_{\mathrm{i}} \int \mathrm{d}\omega_{\mathrm{s}}' \int \mathrm{d}\omega_{\mathrm{i}}' \left[\phi\left(\omega_{\mathrm{s}}, \omega_{\mathrm{i}}\right) \phi\left(\omega_{\mathrm{s}}', \omega_{\mathrm{i}}'\right) \phi^*\left(\omega_{\mathrm{s}}, \omega_{\mathrm{i}}'\right) \phi^*\left(\omega_{\mathrm{s}}', \omega_{\mathrm{i}}\right)\right]. \tag{12}$$

It can be observed that the spectral purity depends on the correlation spectral distribution function $\phi(\omega_{\mathrm{s}}, \omega_{\mathrm{i}})$. According to Eq. (6), $\phi(\omega_{\mathrm{s}}, \omega_{\mathrm{i}})$ primarily depends on the resonant lineshape of the pump, signal, and idler light. The quality factor, which influences the bandwidth of the microring's resonance spectrum, thereby affects the spectral purity. Consequently, the quality factors of the pump, signal, and idler light can significantly impact the spectral purity. Numerical simulations show that the spectral purity increases with $Q_{\mathrm{s(i)}}/Q_{\mathrm{p}}$, reaching 93% at $Q_{\mathrm{s(i)}}/Q_{\mathrm{p}} = 1$ and approaching 99% at $Q_{\mathrm{s(i)}}/Q_{\mathrm{p}} = 3$, as shown in Fig. 4(b).

To meet the varying requirements for the quality factors of the pump and signal (idler) photons in terms of PGR, heralding efficiency, and spectral purity, we have designed and fabricated the cascaded AMZI interferometer-coupled microring. The quality factor of the cascaded AMZI interferometer-coupled microring can be expressed as

$$\frac{1}{Q_v} = \frac{1}{Q_{\mathrm{int},v}} + \frac{1}{Q_{\mathrm{ext},v}}, \tag{13}$$

where Q_{t}, Q_{int}, and Q_{ext} represent the total, intrinsic, and external quality factors, respectively, with the subscript v denoting the pump, signal, or idler. The total quality factor of a microring resonator is determined by two components: the intrinsic quality factor Q_{int} and the external quality factor Q_{ext}. The intrinsic quality factor is given by $Q_{\mathrm{int}} = \omega/V_{\mathrm{g}}\alpha$, where ω is the angular frequency, V_{g} is the group velocity, and α is the round-trip loss coefficient of the microring. It characterizes the energy decay due to intrinsic losses within the resonator. On the other hand, the external quality factor is defined as $Q_{\mathrm{ext}} = \omega L/(V_{\mathrm{g}}|\kappa_{\mathrm{e}}|^2)$, where L is the microring's circumference, and κ_{e} represents the effective cross-coupling coefficient between the resonator and the external environment. The external quality factor describes the loss associated with the exchange of energy between the resonator and the external system through coupling. As the coupling strength increases, the external quality factor Q_{ext} decreases, leading to faster energy escape from the resonator. Based on the theoretical frameworks of all-pass microring resonators and AMZIs,[14] the effective cross-coupling coefficient κ_{e} for the cascaded AMZI-coupled microring can be expressed as

$$|\kappa_{\mathrm{e}}|^2 = 3t^4\kappa^2 + \kappa^6 + 2t^4\kappa^2[\cos(\phi_1+\phi_2) + \cos\phi_1 + \cos\phi_2] - 2t^2\kappa^4[\cos(\phi_1-\phi_2) + \cos\phi_1 + \cos\phi_2], \tag{14}$$

where $\phi_j = \beta\Delta L + \theta_j$, β is the wavelength-dependent propagation constant, ΔL is the arm length difference that determines the interferometer period, and θ_j is the modulation phase controlled by the voltage applied to the thermo-optic phase shifter. Therefore, the quality factors corresponding to different resonance wavelengths in this microring structure can be tuned by designing different arm length differences and adjusting the tunable phases.

In practical SFWM applications based on microrings, the quality factors for the pump and signal (or idler) must be optimized separately. For an SFWM process requiring pump and signal (or idler) quality factors Q_{p} and $Q_{\mathrm{s(i)}}$, assuming a fixed intrinsic

quality factor Q_{int}, the corresponding external coupling coefficients $\left|\kappa_{\text{e,p}}\right|^2$ and $\left|\kappa_{\text{e,s(i)}}\right|^2$ can be independently tuned by adjusting the phases ϕ_1 and ϕ_2, as shown in Figs. 1(d) and 1(e). From Eq. (14), the formula for $|\kappa_{\text{e}}|^2$ can be written as follows:

$$\begin{aligned}|\kappa_{\text{e}}|^2 &= 3t^4\kappa^2+\kappa^6+2t^2\kappa^2\left[t^2\cos(\phi_1+\phi_2)+t^2\cos\phi_1+t^2\cos\phi_2-\kappa^2\cos(\phi_1-\phi_2)-\kappa^2\cos\phi_1-\kappa^2\cos\phi_2\right]\\ &= 3t^4\kappa^2+\kappa^6+2t^2\kappa^2\cdot Y(\phi_1,\phi_2),\end{aligned} \tag{15}$$

where

$$Y(\phi_1,\phi_2)=\left(t^2-\kappa^2\right)(\cos\phi_1+\cos\phi_2+\cos\phi_1\cos\phi_2)-\sin\phi_1\sin\phi_2. \tag{16}$$

The term $Y(\phi_1,\phi_2)$ represents the part of $|\kappa_{\text{e}}|^2$ that is dependent on the adjustable phases. Solving the following system of equations:

$$\begin{aligned}\frac{\partial Y}{\partial\phi_1}&=\left(t^2-\kappa^2\right)(-\sin\phi_1-\sin\phi_1\cos\phi_2)-\cos\phi_1\sin\phi_2=0,\\ \frac{\partial Y}{\partial\phi_2}&=\left(t^2-\kappa^2\right)(-\sin\phi_2-\sin\phi_2\cos\phi_1)-\cos\phi_2\sin\phi_1=0,\end{aligned} \tag{17}$$

we obtain the extreme values of $Y(\phi_1,\phi_2)$ and the corresponding conditions

$$Y=\begin{cases}\dfrac{-4t^4+2t^2-1}{2t^2}, & \phi_1=\phi_2=\arccos\dfrac{1-2t^2}{2t^2},\\ 3\left(t^2-\kappa^2\right), & \phi_1=\phi_2=0,\\ \kappa^2-t^2, & \phi_1=\phi_2=\pi.\end{cases} \tag{18}$$

From this, we find

$$|\kappa_{\text{e}}|^2=\begin{cases}0, & \phi_1=\phi_2=\arccos\dfrac{1-2t^2}{2t^2},\\ \kappa^2\left(4t^2-1\right)^2, & \phi_1=\phi_2=0,\\ \kappa^2, & \phi_1=\phi_2=\pi.\end{cases} \tag{19}$$

When $\phi_1=\phi_2=\arccos((1-2t^2))/2t^2$, the extreme value of $|\kappa_{\text{e}}|^2$ is 0, indicating that there is no overall coupling effect between the waveguide and the microring. Due to the continuity of the values, $|\kappa_{\text{e}}|^2$ can approach this minimal value as the external quality factor increases, making the total quality factor approach the internal quality factor.

When $\phi_1=\phi_2=0$, the extreme value of $|\kappa_{\text{e}}|^2$ is $\kappa^2\left(4t^2-1\right)^2$. Typically, for smaller microring radii, the coupling region is shorter, and the coupling ratio of the curved waveguide is weaker compared to the straight waveguide for the same coupling distance. Therefore, it is usually the case that $0<\kappa\ll 1$ and $t\approx 1$, leading to a value of $|\kappa_{\text{e}}|^2$ that tends to $9\kappa^2$, representing the maximum value. In this scenario, the external quality factor of the microring is minimized, and the total quality factor is also minimal.

When $\phi_1=\phi_2=\pi$, $|\kappa_{\text{e}}|^2$ reaches its extreme value κ^2. At this point, the effective cross-coupling coefficient equals the cross-coupling coefficient of a single coupling region. The cascaded Mach–Zehnder interferometer-coupled microring structure degenerates into an all-pass microring structure with only a single coupling point.

In summary, the range of possible values for $|\kappa_{\text{e}}|^2$ is $[0,9\kappa^2)$. Thus, under the influence of the cascaded Mach–Zehnder interferometer, the microring structure exhibits a significant tunable range for $|\kappa_{\text{e}}|^2$. In practical applications based on four-wave mixing, we need to independently adjust the quality factors of the pump and signal (idler) photons. By relating the internal and external quality factors to the effective coupling efficiency, the corresponding $\left|\kappa_{\text{e,p}}\right|^2$ and $\left|\kappa_{\text{e,s(i)}}\right|^2$ values can be solved for based on the external quality factor of the four-wave mixing process, leading to the appropriate adjustment of the phases ϕ_1 and ϕ_2. That is, for the cascaded Mach–Zehnder interferometer-coupled microring structure, the independent adjustment of $\left|\kappa_{\text{e,p}}\right|^2$ and $\left|\kappa_{\text{e,s(i)}}\right|^2$ can be achieved by tuning the phases ϕ_1 and ϕ_2, thereby independently controlling the quality factors Q_{p} and $Q_{\text{s(i)}}$ for the pump and signal (idler) photons. From Eq. (15), we derive the phase conditions corresponding to the values of $\left|\kappa_{\text{e,p}}\right|^2$ and $\left|\kappa_{\text{e,s(i)}}\right|^2$:

$$\phi_1=(a+b)/2,\quad \phi_2=(a-b)/2, \tag{20}$$

where

$$\begin{aligned}a&=\arccos\left(\pm\frac{1}{2}\sqrt{\frac{\left|\kappa_{\text{e,p}}\right|^2+\left|\kappa_{\text{e,s(i)}}\right|^2}{2t^4\kappa^2}-1}\right),\\ b&=\arccos\left(\frac{\left|\kappa_{\text{e,p}}\right|^2-\left|\kappa_{\text{e,s(i)}}\right|^2}{a\cdot 8t^4\kappa^2}\right).\end{aligned} \tag{21}$$

The constraint conditions are

$$\begin{aligned}&2t^4\kappa^2\le\left|\kappa_{\text{e,p}}\right|^2-\left|\kappa_{\text{e,s(i)}}\right|^2\le 10t^4\kappa^2,\\ &\left(\frac{\left(\left|\kappa_{\text{e,p}}\right|^2-\left|\kappa_{\text{e,s(i)}}\right|^2\right)^2}{8t^4\kappa^2\left(\left|\kappa_{\text{e,p}}\right|^2+\left|\kappa_{\text{e,s(i)}}\right|^2\right)-16t^8\kappa^4}\right)^2\le 1.\end{aligned} \tag{22}$$

These equations provide the constraint conditions for $\left|\kappa_{\text{e,p}}\right|^2$ and $\left|\kappa_{\text{e,s(i)}}\right|^2$, meaning that the quality factors corresponding to the pump and signal (idler) photon wavelengths in this structure have a limited tunable range, as shown in Fig. 1(c). When κ_{e} reaches its minimum value of 0, the Q factor is maximized, while the maximum κ_{e} corresponds to the minimum Q factor. As the self-coupling coefficient t increases, κ_{e} decreases, shifting the adjustment range toward higher Q factor. Conversely, as t decreases, the adjustment

range moves toward lower Q factor. Depending on the value of $Q_{\rm int}/Q_{\rm ext}$, the microring can operate in three coupling regimes. Specifically, when $Q_{\rm int}/Q_{\rm ext}=1$, the microring achieves critical coupling, with nearly zero transmission as the resonator completely absorbs the light. When $Q_{\rm int}/Q_{\rm ext}>1$, the microring is overcoupled, with $|\kappa_{\rm e}|^2>\alpha L$, and when $Q_{\rm int}/Q_{\rm ext}<1$, the microring is undercoupled, with $|\kappa_{\rm e}|^2<\alpha L$. In both the overcoupled and undercoupled regimes, the transmission at resonance is non-zero, and the resonance bandwidth differs: overcoupled microrings have a larger bandwidth, while undercoupled microrings have a narrower bandwidth. We have divided Fig. 1(c) into four regions, and Table 1 summarizes the characteristics of each region.

Table 1. Classification of the variation ranges of pump and signal (idler) photon quality factors based on the coupling states.

Region	Pump light	Signal (Idler) light	Application
I	under-coupled	under-coupled	–
II	over-coupled	under-coupled	optimizing spectral purity
III	over-coupled	over-coupled	optimizing PGR, HE
IV	under-coupled	over-coupled	optimizing PGR, HE

In comparisons with PGR, HE, and spectral purity, we have summarized their respective optimization conditions in Table 2. As observed, under continuous wave pumping, the spectral purity cannot reach a high value due to the narrow linewidth of the pump light. Therefore, only HE and PGR are considered in this case. The PGR exhibits a clear optimal condition, and the over-coupling condition for the signal (idler) light also applies to the optimization of HE. However, as the ratio $Q_{\rm int,s(i)}/Q_{\rm ext,s(i)}$ continues to increase, HE improves, while PGR gradually decreases. Therefore, when $Q_{\rm int,p}/Q_{\rm ext,p}=1$, and $Q_{\rm int,s(i)}/Q_{\rm ext,s(i)}$ is within the range of 2 and slightly above 2, both HE and PGR can be effectively optimized. Under pulsed light pumping, HE still improves with an increasing $Q_{\rm int,s(i)}/Q_{\rm ext,s(i)}$, and the optimal point for PGR lies in a higher over-coupling state. In regions where both $Q_{\rm int,s(i)}/Q_{\rm ext,s(i)}$ and $Q_{\rm int,p}/Q_{\rm ext,p}$ are large, areas with a high $Q_{\rm s(i)}/Q_{\rm p}$ ratio can simultaneously achieve optimization of spectral purity. However, due to the current limitations in the tunability of the quality factor for the chips used in the experiment, it has not yet been possible to achieve this in practice.

Table 2. Comparisons of optimization conditions for PGR, HE, and spectral purity.

Optimization criteria	Pump	Optimization conditions
PGR	CW pulse	$Q_{\rm int,p}/Q_{\rm ext,p}=1, Q_{\rm int,s(i)}/Q_{\rm ext,s(i)}=2$ $Q_{\rm int,p}/Q_{\rm ext,p}\approx 10.9, Q_{\rm int,s(i)}/Q_{\rm ext,s(i)}\approx 4.6$[10]
HE	CW pulse	maximize $Q_{\rm int,s(i)}/Q_{\rm ext,s(i)}$ maximize $Q_{\rm int,s(i)}/Q_{\rm ext,s(i)}$
Spectral purity	CW pulse	– maximize $Q_{\rm s(i)}/Q_{\rm p}$

3. Experiment and result

In our experiments, we fabricated an MRR coupled with cascaded AMZIs on a silicon-on-insulator (SOI) chip. The waveguide cross-section was 500 nm × 220 nm, while the microring radius R was 28 μm, corresponding to a free spectral range (FSR) of approximately 3.2 nm (400 GHz), compatible with commercial dense wavelength-division multiplexing (DWDM) systems. The arm length difference of the two AMZIs was designed as $\Delta L=\pi R$, and the bending radius in the coupling region matched the microring radius. The coupling gap g between the microring and interferometers was set to 180 nm. The structure includes a total of three thermo-optic phase modulators: two placed on the long arms of the interferometer to control the effective coupling coefficients, and one on the microring to adjust the resonance wavelength of the microring. Each modulator was connected to a circuit board and controlled by an external voltage source.

The experimental setup for measuring the PGR is shown in Fig. 2(a). A tunable continuous-wave (CW) laser (FWHM = 400 kHz, wavelength tuning range 1500 nm–1630 nm) was used as the pump source. The output laser was filtered by a DWDM and passed through a polarization controller (PC) before coupling into the silicon chip via an on-chip grating coupler, with a coupling loss of approximately 7.5 dB. The microring resonance wavelengths were precisely aligned with the DWDM channel centers by adjusting the thermo-optic phase modulators. The pump, signal, and idler wavelengths were selected as 1552.5 nm (CH31), 1549.3 nm (CH35), and 1555.8 nm (CH27), respectively. The polarization controller ensured mode matching between the pump light and the grating coupler on the silicon chip. The insertion loss of the polarization controller is approximately 0.37 dB. After entering the microring, the pump light underwent SFWM, and the resulting photons were decoupled from the chip through the grating coupler, passing through subsequent filtering stages. The total coupling and decoupling loss of the silicon chip was approximately 15 dB. The chip temperature was stabilized using a thermoelectric cooler (TEC) with a feedback controller, providing a precision of 0.01 °C. The thermo-optic modulators were controlled by a digital-to-analog converter (DAC) with eight voltage channels and a resolution of 0.01 V.

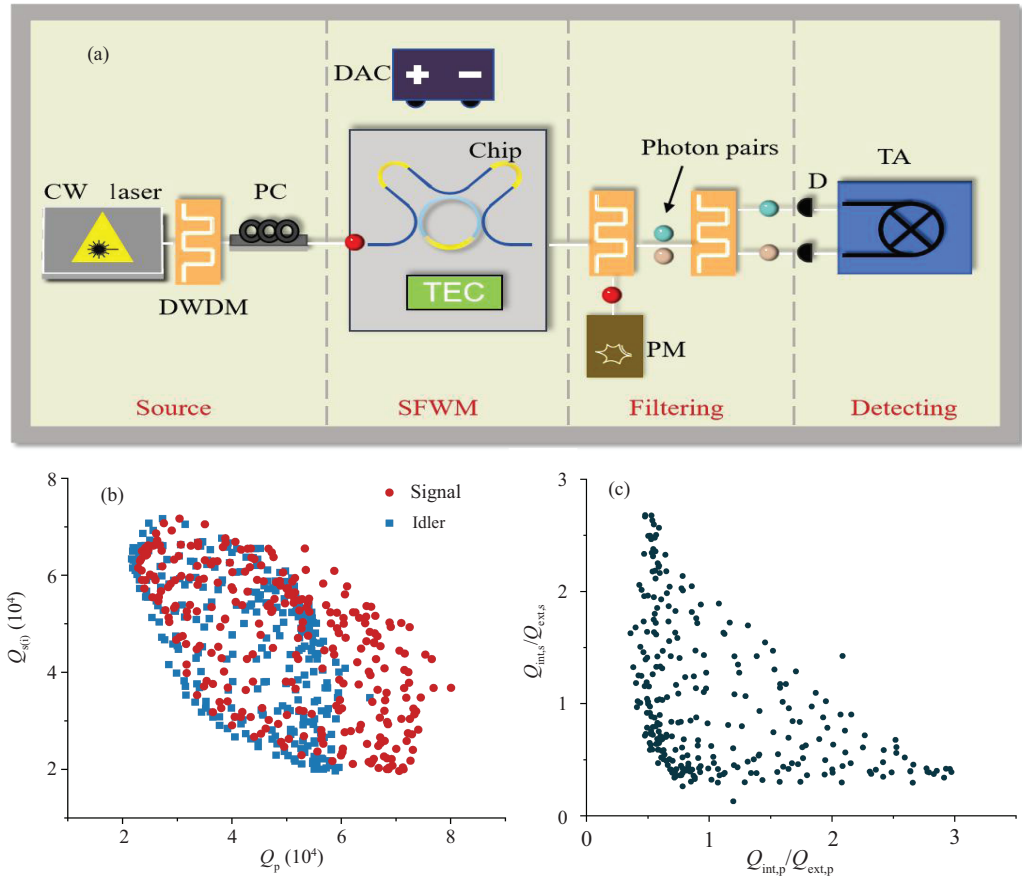


Fig. 2. (a) Experimental setup for PGR measurement. PC: polarization controller; PM: power meter; D: superconducting nanowire single-photon detector (SNSPD); TEC: temperature controller; DAC: digital-to-analog converter; DWDM: dense wavelength-division multiplexer; TA: time analyzer. (b) Experimentally obtained tunable ranges of Q_p and $Q_{s(i)}$ for the cascaded AMZI-coupled microring resonator. Blue squares represent the corresponding values of Q_p and Q_i, while red circles indicate the corresponding values of Q_p and Q_s. (c) The experimentally measured ranges of $Q_{int,s(i)}/Q_{ext,s(i)}$ and $Q_{int,p}/Q_{ext,p}$.

A two-stage DWDM filter (The total insertion loss is 5.8 dB) was used to separate the pump, signal, and idler photons. The pump power was measured using a power meter, while the signal and idler photons were detected using SNSPDs. The SNSPDs had dark count rates of 150 Hz and detection efficiencies of 74% and 75%, respectively. A time analyzer with a time bin width of 78 ps was used to record coincidence counts.To measure the transmission spectrum of the microring, the tunable CW laser was scanned over a range of ± 0.25 nm around the resonance wavelengths 1552.5 nm, 1549.3 nm, and 1555.8 nm, with a resolution of 0.002 nm. We varied the voltage combinations applied to the two AMZIs to adjust the phases θ_1 and θ_2, performing transmission spectrum scans for each set of parameters. The voltages ranged from $\sqrt{0}$ V to $\sqrt{48}$ V, with increments of $\sqrt{3}$ V, resulting in a total of $17 \times 17 = 289$ combinations for the two phases. The linewidths were then obtained by fitting the Lorentzian profiles, from which the quality factors at each resonant wavelength were extracted. Since the AMZI arm length difference $\Delta L = \pi R$ results in an interference period twice that of the microring, the signal and idler photons, corresponding to resonance wavelengths separated by twice the FSR, exhibited similar quality factors and trends under different phase settings. Based on the measured quality factors for the pump and signal (idler) photons at different phase settings, we obtained the tunable range of quality factors for the microring structure, as shown in Figs. 2(b) and 2(c). The results indicate a wide tunability of the quality factors, demonstrating the versatility of the cascaded AMZI-coupled design.

We next investigated the optimization of the PGR at a fixed pump power. Using the theoretical relationship between PGR and the quality factors of the pump and signal (idler) photons, combined with the measured tunable ranges of quality factors, we calculated the theoretical tunable range of PGR for this structure, as shown in Fig. 3(a). Experimentally, the pump wavelength was aligned with the microring resonance, and the pump power was fixed at 1 mW. Thermal crosstalk from the phase modulators caused slight shifts in the resonance wavelengths, which were corrected during the measurements. Under an on-chip pump power of 100 μW, the maximum directly measured coincidence count rate was 92 Hz. After accounting for losses, the PGR was determined to be 1.32 MHz/mW^2. This was achieved with $Q_{int,s(i)}/Q_{ext,s(i)} = 1.93$ and $Q_{int,p}/Q_{ext,p} = 0.88$. The final normalized coincidence counting results are shown in Fig. 3(b). The experimental results closely match the theoretical predictions. The maximum PGR was achieved when the pump photon was critically coupled, while the signal and idler photons were overcoupled. These results confirm that the cascaded AMZI-coupled microring structure enables the independent tuning of the quality

factors to achieve the optimal conditions for photon-pair generations.

For continuous-wave pumping, the heralding efficiency (HE) of the photon-pair source is optimized. By using Eq. (11) and the range of quality factors for the pump and signal (idler) photons obtained from transmission spectrum measurements of the microring structure, we can derive the theoretical range of HE for this setup, as shown in Fig. 3(c). Based on experimentally measured signal-idler photon pair counts and single-photon counting rates, and after accounting for grating coupling losses, out-of-chip optical path losses, dark count noise, and other factors, we combine these results with Eq. (11) to obtain the relationship between HE and $Q_{\mathrm{int,s(i)}}/Q_{\mathrm{ext,s(i)}}$, as shown in Fig. 3(d). The data indicates that HE increases with $Q_{\mathrm{int,s(i)}}/Q_{\mathrm{ext,s(i)}}$, in agreement with theoretical expectations. The difference between the theoretical and experimental values is primarily due to residual pump light, sideband noise, Raman noise, and other unfiltered factors.

To evaluate the photon spectral purity, we used the experimental setup shown in Fig. 4(a). A wavelength-tunable pulsed laser (FWHM = 1.19 nm) was used as the pump source. After filtering through a DWDM module, the pump power was maximized using a polarization controller before being coupled into the chip. The SFWM-generated signal and idler photons, along with the residual pump light, were decoupled from the chip via the grating coupler and sent to a filtering module. The filtering module first isolated the signal photons using a DWDM filter, then split them into two paths using a 50 : 50 beam splitter, followed by tunable filters before entering the SNSPDs for coincidence detection. The tunable filters allowed independent control of the center wavelength and bandwidth, with a tuning range of 1525 nm–1610 nm and a minimum bandwidth of 0.08 nm. At a bandwidth of 0.2 nm, the insertion loss was approximately 6 dB. Since the tunable filter bandwidth was much larger than the signal photon linewidth, it introduced no spectral filtering.

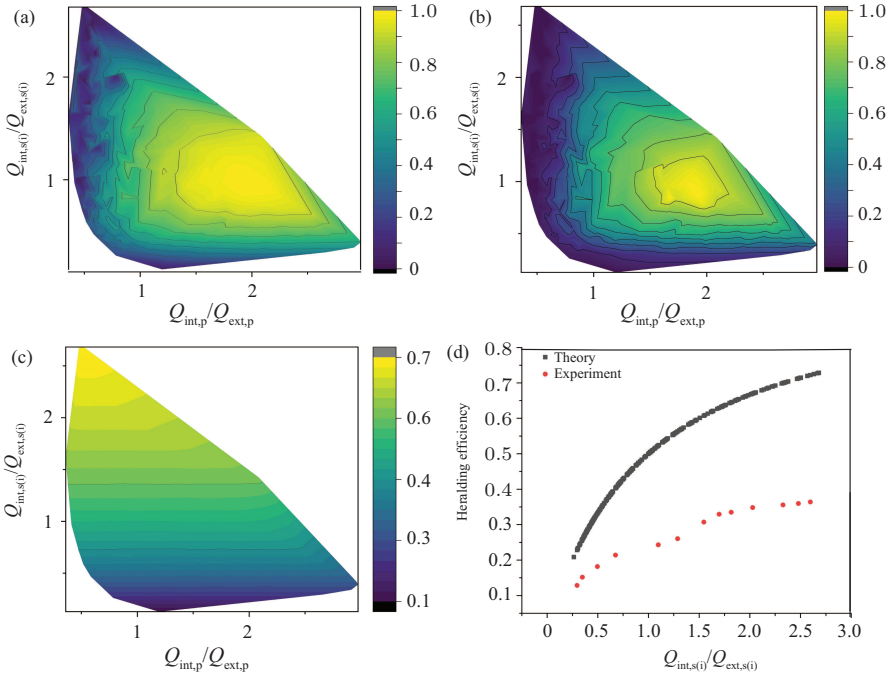


Fig. 3. (a) Theoretically simulated normalized PGR based on the experimentally obtained tunable ranges of $Q_{\mathrm{int,p}}/Q_{\mathrm{ext,p}}$ and $Q_{\mathrm{int,s(i)}}/Q_{\mathrm{ext,s(i)}}$, showing its dependence on $Q_{\mathrm{int,s(i)}}/Q_{\mathrm{ext,s(i)}}$ and $Q_{\mathrm{int,p}}/Q_{\mathrm{ext,p}}$. (b) Experimentally measured normalized PGR as a function of $Q_{\mathrm{int,s(i)}}/Q_{\mathrm{ext,s(i)}}$ and $Q_{\mathrm{int,p}}/Q_{\mathrm{ext,p}}$. (c) Theoretically simulated HE based on the experimentally obtained tunable ranges of $Q_{\mathrm{int,p}}/Q_{\mathrm{ext,p}}$ and $Q_{\mathrm{int,s(i)}}/Q_{\mathrm{ext,s(i)}}$, showing its dependence on $Q_{\mathrm{int,s(i)}}/Q_{\mathrm{ext,s(i)}}$. (d) Experimentally measured HE as a function of $Q_{\mathrm{int,s(i)}}/Q_{\mathrm{ext,s(i)}}$.

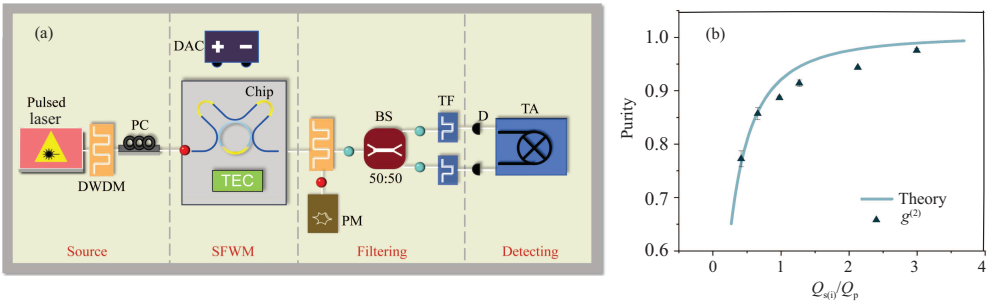


Fig. 4. (a) Experimental setup for photon spectral purity measurement via time-integrated second-order correlation. BS: beam splitter; TF: tunable filter. (b) Theoretical and experimentally measured photon spectral purity, derived from $g^{(2)}$ measurements, as a function of $Q_{\mathrm{s(i)}}/Q_{\mathrm{p}}$.

Table 3. Spectral purity measurement results.

	i	ii	iii	iv	v	vi
$Q_{s(i)}/Q_p$	0.414	0.658	0.977	1.269	2.128	2.995
Purity	77.25% ± 1.5%	85.72% ± 1.1%	88.69% ± 0.3%	91.41% ± 0.6%	94.37% ± 0.3%	97.55% ± 0.4%

The spectral purity was evaluated through time-integrated second-order correlation measurements $g^{(2)}$.[26] Before the spectral purity measurements, the quality factors for various voltage combinations were obtained from the transmission spectra. Six voltage combinations within the tunable quality factor range were selected for the purity measurements. By recording the single-photon counts and coincidence counts from the SNSPDs, the second-order correlation $g^{(2)}$ of the signal photons was calculated. The spectral purity results derived from the second-order correlation measurements are shown in Fig. 4(b) and Table 3. The measured purity trends as a function of $Q_{s(i)}/Q_p$ agree well with the theoretical predictions. These results demonstrate that the cascaded AMZI-coupled microring structure enables independent tuning of the quality factors for pump and converted photons, thereby optimizing the photon spectral purity.

4. Discussion and conclusion

In summary, we have proposed a cascaded AMZI-coupled microring structure that enables independent and wide-range tuning of the quality factors for pump, signal, and idler photons. This structure provides the flexibility to meet various coupling and quality factor requirements for different optical processes. Based on this design, we implemented a silicon photonic chip and experimentally demonstrated its performance in optimizing photon-pair generation rates and photon spectral purity. The experimental results show excellent agreement with theoretical predictions, highlighting the effectiveness and reliability of the proposed structure.The results further demonstrate the multi-degree-of-freedom tunability of the microring chip, which can achieve precise control across a range of applications. This dynamic, highly tunable microring platform not only provides a versatile solution for quantum optics applications but also addresses diverse requirements in nonlinear optical processes. By integrating tunable control and compatibility with standard silicon photonics platforms, this work offers a significant step forward in the development of multifunctional, high-performance photonic devices for both quantum and classical optical technologies.

Acknowledgements

Project supported by the Innovation Program for Quantum Science and Technology (Grant No. 2021ZD0301500) and the National Natural Science Foundation of China (Grant No. 62105366).

References

[1] Xu F H, Ma X F, Zhang Q, Lo H K and Pan J W 2020 *Rev. Mod. Phys.* **92** 025002
[2] Zhong H S, Wang H, Deng Y H, Chen M C, Peng L C, Luo Y H, Qin J, Wu D, Ding X, Hu Y, Hu P, Yang X Y, Zhang W J, Li H, Li Y, Jiang X, Gan L, Yang G, You L, Wang Z, Li L, Liu N L, Lu C Y and Pan J W 2020 *Science* **370** 1460
[3] Vos K D, Bartolozzi I, Schacht E, Bienstman P and Baets R 2007 *Opt. Express* **15** 7610
[4] Sharping J E, Lee K F, Foster M A, Turner A C, Schmidt B S, Lipson M, Gaeta A L and Kumar P 2006 *Opt. Express* **14** 12388
[5] Silverstone J W, Bonneau D, Ohira K, *et al.* 2014 *Nat. Photon.* **8** 104
[6] Shacham A, Bergman K and Carloni L P 2008 *IEEE Trans. Comput.* **57** 1246
[7] Zhang Q Y, Xu P and Zhu S N 2018 *Chin. Phys. B* **27** 054207
[8] Bao J M, Fu Z R, Pramanik T, *et al.* 2023 *Nat. Photon.* **17** 573
[9] Fiorentino M, Voss P L, Sharping J E and Kumar P 2002 *IEEE Photon. Technol. Lett.* **14** 983
[10] Wu C, Liu Y W, Wang Y, *et al.* 2022 *Opt. Express* **30** 9992
[11] Kwiat P G, Waks E, White A G, Appelbaum I and Eberhard P H 1999 *Phys. Rev. A* **60** R773
[12] Kaneda F, Christensen B G, Wong J J, Park H S, McCusker K T and Kwiat P G 2015 *Optica* **2** 1010
[13] Matthews J C F, Politi A, Stefanov A and O'brien J L 2009 *Nat. Photon.* **3** 346
[14] Barbarossa G, Matteo A M and Armenise M N 1995 *J. Lightwave Technol.* **13** 148
[15] Cai M, Painter O and Vahala K J 2000 *Phys. Rev. Lett.* **85** 74
[16] Tison C C, Steidle J A, Fanto M L, Wang Z, Mogent N A, Rizzo A, Preble S F and Alsing P M 2017 *Opt. Express* **25** 33088
[17] Silverstone J W, Santagati R, Bonneau D, Strain M J, Sorel M, O'Brien J L and Thompson M G 2015 *Nat. Commun.* **6** 7948
[18] Liu Y W, Wu C, Gu X W, *et al.* 2019 *Opt. Lett.* **1** 73
[19] Wu C, Liu Y W, Gu X W, *et al.* 2020 *Sci. China-Phys., Mech. Astron.* **63** 220362
[20] Zheng Q L, Liu J C, Wu C, *et al.* 2022 *Chin. Phys. B* **31** 024206
[21] Vernon Z, Menotti M, Tison C C, *et al.* 2017 *Opt. Lett.* **42** 3638
[22] Heuck M, Pant M, and Englund D R 2018 *New J. Phys.* **20** 063046
[23] Wu C, Liu Y W, Gu X W, Xue S C, Yu X X, Kong Y C, Qiang X G, Wu J J, Zhu Z H and Xu P 2019 *Chin. Phys. B* **28** 104211
[24] Guo K, Shi X D, Wang X L, Yang J B, Ding Y H, Ou H Y and Zhao Y J 2018 *Photon. Res.* **6** 587
[25] Gatti A, Corti T, Brambilla E and Horoshko D 2012 *Phys. Rev. A* **86** 053803
[26] Christ A, Laiho K, Eckstein A, Cassemiro K N and Silberhorn C 2011 *New J. Phys.* **13** 033027